Dalton Transactions

ROYAL SOCIETY OF CHEMISTRY

PAPER

View Article Online
View Journal | View Issue

Cite this: *Dalton Trans.*, 2025, **54**, 14384

Compositional design rules for tuning functionalities in $CuInP_2X_6$ (X = S, Se) van der Waals semiconductor ferroelectrics

Mona Layegh and Joseph W. Bennett *

Two-dimensional van der Waals (2D-vdW) semiconducting ferroelectrics, such as $CuInP_2Se_6$ (CIPSe) and $CuInP_2S_6$ (CIPS), offer unique opportunities for lightweight, scalable, low-power nanoscale electronic devices. However, the limited pool of functional 2D-vdW ferroics highlights the need for clear design principles that can be used to guide experiments. Here, we use first-principles density functional theory (DFT) to study how isovalent atomistic substitution at In and P sites modifies structure, polarization, and electronic properties in CIPSe and CIPS. When substituting In with Sb and Bi, and P with As and Sb, we reveal how ionic radius mismatch, electronegativity differences, and stereochemical lone pair activity shape the ferroelectric and semiconducting response in both rigid (S-based) and soft (Se-based) 2D lattices. In CIPSe, Bi doping at In sites widens the band gap to ~1.07 eV without reducing polarization or switching performance, provided the Bi atoms are placed in a balanced zigzag arrangement that limits local strain. In CIPS, polarization values drop more noticeably than in CIPSe, and dopant location has a stronger effect on switching behavior. P-site substitution leads to stronger distortions in CIPSe, where larger dopants destabilize the P–P dimer network and in many instances, we predict it to be a metal. However, with As doping in CIPS, polarization remains stable, and the band gap decreases without major structural disruption. Our results establish structure–property design rules based on dopant size and location, host lattice stiffness, and chemical compatibility, offering a route to engineer new 2D ferroelectrics in which polarization and band gap can be tuned together through specific compositional changes.

Received 16th July 2025,
Accepted 1st September 2025

DOI: 10.1039/d5dt01674f

rsc.li/dalton

1. Introduction

The growing demand for electronic devices that are thinner, more lightweight, and energy-efficient has intensified the search for materials that support size, weight, and power (SWaP) optimization. Two-dimensional van der Waals (vdW) semiconducting materials have emerged as promising candidates due to their large surface area, chemical stability, and compositional tunability.[1–3] Among them, $CuInP_2Se_6$ (CIPSe) and $CuInP_2S_6$ (CIPS) uniquely combine semiconducting and ferroelectric properties, offering exceptional versatility for energy systems, electronics, and photonics.[4–8] Despite their structural similarities, CIPSe and CIPS exhibit distinct physical properties. CIPSe shows a lower ferroelectric transition temperature (~230 K)[9] and a broader phase transition window compared to the sharper, higher-temperature transition (~305 K)[7] observed in CIPS.[7,9,10] These differences translate into complementary functionalities. CIPSe, with broadband UV–visible absorption, low dark current, and X-ray sensitivity, is well-suited for high-performance photodetectors and imaging applications,[11] while CIPS, with greater polarization stability, is favored for energy harvesting and capacitor applications.[12] Together, they provide a foundation for exploring compositional tuning strategies to broaden functional applications. Tuning ferroelectric and semiconducting properties simultaneously opens a pathway to multifunctional design, particularly for devices coupling multiple order parameters, such as light and polarization in ferroelectric photovoltaics, or magnetization and polarization in multiferroics,[13,14] with recent studies emphasizing that in CIPS, photocatalytic performance depends sensitively on both polarization and electronic band structure.[15] Prior studies showed that Cr substitution at the In site results in antiferroelectric–antiferromagnetic behavior,[16–18] but no ferromagnetic or ferroelectric phases with In and Cr have yet been realized. Related layered compounds like $CuSbP_2Se_6$ and $AgBiP_2Se_6$ have demonstrated semiconductivity and anisotropic responses,[19] yet systematic studies on Sb/Bi doping in sulfur-based compounds, or substitutions targeting the dimeric P–P units, remain unexplored.

There are 5 structure types in the ICSD which contain both ferroics like the quaternary compositions mentioned in the

Department of Chemistry & Biochemistry, University of Maryland Baltimore County, Baltimore, MD 21250, USA. E-mail: bennettj@umbc.edu

last paragraph and the phosphochalcogenide unit: $FePS_3$, $FePSe_3$, $AgInP_2S_6$, $AgVP_2S_6$, and $AgVP_2Se_6$.[20] The compositions that we find in these structure types include antiferroelectrics such as $CuCrP_2Se_6$ and $CuBiP_2Se_6$ [21,22] and a few entries with disordered S and Se, *i.e.* $NiPS(Se)_3$.[23] There remains a dearth of knowledge on how cation substitutions that include the main group cations P and In could affect the functional and electronic properties. Here, we address these knowledge gaps by exploring systematic atomistic substitutions guided by ionic radii trends and electronic configuration considerations. By substituting In^{3+} (0.80 Å) with Sb^{3+} (0.76 Å) or Bi^{3+} (1.03 Å), and P^{4+} (~0.41 Å) with As^{4+} (~0.52 Å) or Sb^{4+} (~0.68 Å), we aim to tune bonding characteristics, lattice distortion, polarization, and electronic band structure. The ionic size mismatch between cations within octahedral (MX_6) and ethane-like units (P_2X_6) within layers of X = S^{2-} (1.84 Å) and Se^{2-} (1.98 Å) anions, specifically between Bi, As, and Sb with In and P, introduces opportunities for controlled local strain, while the stereochemical lone pair activity of Bi can further modulate distortion and electronic behavior.[24,25] These deliberate isovalent main group p-block chemical substitutions form the core of this study, enabling band gap tuning while preserving or selectively altering polarization in layered vdW ferroelectrics.

Despite significant progress in understanding CIPSe and CIPS, certain gaps remain in the literature. For instance, while the broader window of transition temperature of CIPSe suggests the potential for tuning, systematic studies on how compositional changes at the In- and P-sites affect its structural, electronic, and ferroelectric properties are limited. Moreover, existing literature primarily focuses on intrinsic properties, leaving opportunities to explore targeted substitutions as a route to property optimization. The primary objectives of this study are to (i) demonstrate how compositional tuning at the In- and P-sites affects the structural, electronic, and ferroelectric properties of CIPS and CIPSe, (ii) understand how cation ordering will affect specific compositions (perfectly alternating *vs.* layering), and (iii) derive design rules to guide next generation 2D vdW ferroelectrics. In employing density functional theory (DFT), we aim to understand how changes in bonding and atomic site configurations will influence polarization, band structure, and other key properties to guide the targeted syntheses of compositionally tuned 2D-vdW materials.

2. Methodology

2.1 Computational details

All first-principles DFT calculations were performed with the open source Quantum ESPRESSO[26,27] (QE) package using the GBRV (Garrity–Bennett–Rabe–Vanderbilt)[28] ultrasoft pseudopotentials.[29] Each of the potentials used was generated with a scalar relativistic calculation. A plane-wave basis set with a kinetic energy cutoff of 40 Ry and a charge density cutoff of 320 Ry was employed, along with a 6 × 6 × 6 Monkhorst–Pack *k*-point grid. Convergence criteria for the total energy (1×10^{-7} Ry) and forces (2×10^{-6} Ry $Bohr^{-1}$) were set to reliably ensure residual forces below 5 meV per Angstrom per atom. The exchange–correlation functional was treated within the generalized gradient approximation (GGA),[30] using the PBE (Perdew–Burke–Ernzerhof) functional. For vdW interactions, the Grimme D2 addition[31] was applied to PBE where indicated, however our choice of using S_6 = 0.5 comes from tuning the parameters of the Grimme D2 vdW addition instead of using the default value of 0.75. Our exchange correlation tests are presented in the supplemental materials. All structural optimizations were performed without any atomic constraints, allowing all atoms to fully relax. Polarization values were calculated using the Berry phase approach[32,33] and electronic band structures were generated following the procedures outlined by Layegh and Bennett,[34] using the publicly available tutorials hosted at GitHub (**https://github.com/bennettlabs-UMBC/Electronic-Band-Structures**).

2.2 Structural models and substitution schemes

In the lattice structures of CIPS and CIPSe, indium (In^{3+}) sits in an octahedral site within the vdW-layered framework, forming weak covalent bonds with phosphorus dimers (P–P) and strong covalent bonds with chalcogen atoms (S or Se), bridging one half the ethane-like $[P_2S_6]^{4-}$ units and contributing to overall charge balance. In contrast, copper (Cu^{1+}) atoms off-center from the octahedral site and can occupy positions as far away from the layer as within the vdW gaps, where they interact less strongly with the lattice and exhibit higher mobility compared to indium. This weaker bonding comes from a competition between vdW forces and covalent bonding, a behavior often seen in ABP_2X_6-type layered materials.[35] Even though they share the same structure, CIPSe exhibits softer, more polarizable bonding than CIPS due to the larger ionic radius of Se^{2-} (1.98 Å) when compared to S^{2-} (1.84 Å), and its lower electronegativity. This leads to longer bonds and increased lattice flexibility. This trend is reflected in the Cu^{1+} atomic displacements, which are smaller in CIPSe compared to CIPS. Fig. 1 illustrates the structure of both the paraelectric and ferroelectric 2D vdW CIPSe investigated here, depicting cation displacements.

Due to the inherent partial octahedral site occupancy of Cu^{1+} and In^{3+} in CIPS, we adopted a structurally similar but fully ordered compound, CIPSe, as a reference framework for constructing ordered analogs. Using CIPSe as the crystallographic scaffold enables systematic evaluation of cation substitution effects without introducing complexities arising from partial site occupancy. This modeling choice is reasonable based on the isostructural nature of the two compounds, their shared trigonal (R3) symmetry, and the chemical similarity between S and Se. Both CIPS and CIPSe undergo symmetry-breaking transitions from centrosymmetric to polar structures during ferroelectric ordering,[36] supporting the validity of CIPSe as a reliable reference framework. While this approach does not account for the full extent of disorder in CIPS, it allows for controlled structural relaxations and meaningful comparison across substitutional variants, providing valuable insights into structure–property relationships in ABP_2X_6-type vdW ferroelectrics.

To examine the role of local chemical environment on ferroelectric polarization and electronic structure we systematically

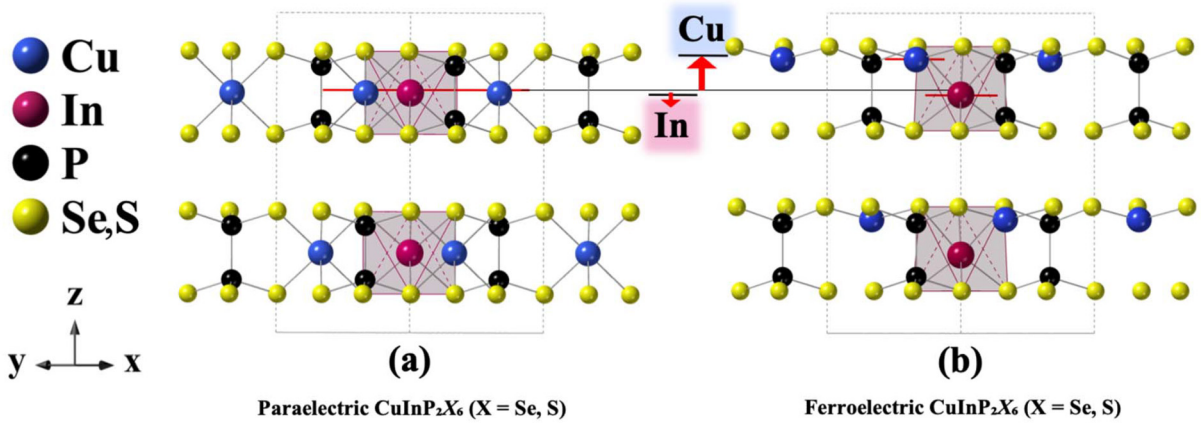

Fig. 1 Relaxed structures of $CuInP_2X_6$ (X = Se, S) in the (a) paraelectric and (b) ferroelectric phases. Displacement of Cu atoms along the *z*-axis breaks the centrosymmetry of the structure, generating a net out-of-plane polarization.

substituted atoms at both the In^{3+} and P^{4+} sites in CIPSe and CIPS. In the trigonal parent structures, In atoms are octahedrally coordinated within vdW-stacked layers and tend to displace from their centrosymmetric positions along the *z*-axis opposite to Cu in the ferroelectric state. Substitution at the In site was performed using Sb and Bi at 25%, 50%, and 75% concentrations to probe the effects of increased ionic size and lone pair activity on lattice distortion. At the P site, each P atom is tetrahedrally coordinated to three chalcogen atoms and one other P atom, forming a symmetric P_2X_6 (X = S, Se) unit. Partial (50%) and full (100%) substitution of P with the larger As atom was performed to see how expanded local geometry influences dimer stability, polarization, and electronic behavior. For 50% substitution at the In site, three symmetry-distinct configurations were generated to represent possible atomic arrangements.

Configuration 1 places all substituent atoms in one layer and all In atoms in the other, forming an interlayer-partitioned structure (Fig. 2a). **Configuration 2** alternates the dopant and host atoms within each layer while maintaining opposite alignment across layers (Fig. 2b). **Configuration 3** features in-plane alternation with interlayer self-pairing, wherein identical atoms face each other across adjacent layers (Fig. 2c). At the P site, 50% substitution with Sb or As yields two distinct configurations. **Configuration A** (Fig. 2d) features full separation of P and dopant atoms, with one layer composed entirely of P–P dimers and the other of dopant–dopant dimers. **Configuration B** (Fig. 2e) introduces intralayer alternation, leading to the formation of mixed P-dopant dimers within each layer. This nomenclature, fully listed in Table 1 will be used throughout the manuscript to distinguish between substitution types, concentrations, and configurational patterns.

3. Results and discussion

3.1 Structural response to chemical substitution

$CuInP_2X_6$ (X = S, Se) materials feature a layered structure where Cu^{1+} and In^{3+} cations are positioned between P–X frameworks within vdW-bonded layers. As described in Section 2.2, In atoms form more rigid covalent networks with P and chalcogen atoms, while Cu atoms occupy more weakly bound positions, making them highly responsive to lattice distortions. In the centrosymmetric (paraelectric) structure (Fig. 1a), Cu atoms sit near the midplane between chalcogen layers, resulting in no net polarization. However, due to weak interlayer bonding, Cu atoms can shift along the out-of-plane (*z*) direction, breaking inversion symmetry and giving rise to a ferroelectric state (Fig. 1b). This polar distortion, driven mainly by Cu displacement relative to the more tightly bound In–P_2X_6 framework, establishes a spontaneous polarization aligned with the layer stacking axis.[37] Understanding how chemical substitution at the In or P sites influences these structural distortions is essential for controlling the ferroelectric and semiconducting properties of these materials. In the following sections, we investigate how compositional tuning at the In and P site influences the structure–property relationships in $CuInP_2X_6$ derivatives. In the paraelectric phase, Cu atoms are nearly symmetrically coordinated to six chalcogen atoms. As the material transitions into the ferroelectric phase, Cu displacement along the *z*-axis breaks this symmetry, strengthening bonds with three chalcogen atoms on one side while stretching and weakening bonds with the opposite layer. This asymmetric coordination is central to generating spontaneous polarization in solid state $CuInP_2X_6$ (X = S, Se) materials.

To highlight the key structural and electronic responses to different substitution strategies, Table 2 includes pristine CIPS and CIPSe references, the best-performing In-site doped structures, and representative P-site doped systems for sulfide and selenide compounds. This selection enables comparison between cases where polarization and semiconducting behavior are (i) preserved, (ii) slightly affected, or (iii) considerably compromised. Table 2 shows that undoped CIPSe has a larger lattice volume and slightly smaller Cu displacement compared to CIPS, consistent with its softer, more polarizable Se lattice. After doping, both systems show volume expansion, but the changes in atomic displacement are more atom specific. In CIPSe, Cu dis-

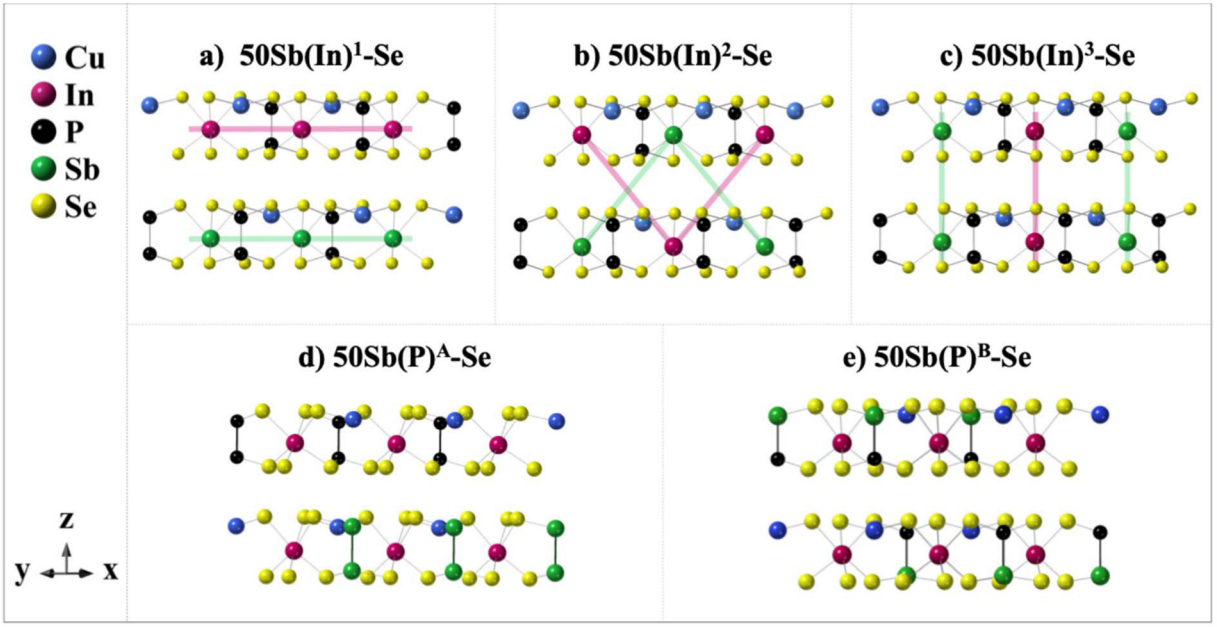

Fig. 2 Atomic configurations of 50% Sb-substituted ferroelectric (polar) phase of CIPSe at the In site and P site, showing symmetry-distinct configurations: (a) fully layer-separated, (b) alternating across layers, (c) alternating within layers, for In-site doping, and (d) layered, (e) mixed for P-site doping. Shaded lines depict the different types of layer ordering in the present study.

Table 1 Configurational nomenclature for doped CIPSe and CIPS structures

System	Substitution site	Dopant	Configurations		
CIPSe	In	Sb	25Sb(In)–Se	$50Sb(In)^{1,2,3}$–Se	75Sb(In)–Se
		Bi	25Bi(In)–Se	$50Bi(In)^{1,2,3}$–Se	75Bi(In)–Se
	P	Sb	$50Sb(P)^{A,B}$–Se		100Sb(P)–Se
		As	$50As(P)^{A,B}$–Se		100As(P)–Se
CIPS	In	Sb	25Sb(In)–S	$50Sb(In)^{1,2,3}$–S	75Sb(In)–S
		Bi	25Bi(In)–S	$50Bi(In)^{1,2,3}$–S	75Bi(In)–S
	P	Sb	$50Sb(P)^{A,B}$–S		100Sb(P)–S
		As	$50As(P)^{A,B}$–S		100As(P)–S

Table 2 Lattice volume, displacement, and electronic structure trends for undoped and representative doped CIPSe and CIPS systems

System	Lattice volume (Å^3)	Symmetry (space group)	Cu Δz (Å, avg ± std)	In Δz (Å, avg ± std)	E_g (eV)
CIPSe (non-polar)	470	$P\bar{3}1c$ (163)	1.48 ± 0.04	−0.01 ± 0.05	0.02
CIPSe (polar)	484	$P31c$ (159)			0.62
50 $Sb(In)^2$-Se	494	Pc (7)	1.46 ± 0.03	−0.01 ± 0.03	0.92
50 $Bi(In)^2$-Se	498	Pc (7)	1.42 ± 0.02	−0.05 ± 0.01	1.07
50 $Sb(P)^A$-Se	514	$P312$ (149)	1.57 ± 0.06	0.04 ± 0.06	0.01
50 $As(P)^A$-Se	495	$P3$ (143)	1.54 ± 0.02	0.01 ± 0.07	0.37
CIPS (non-polar)	416	$P\bar{3}1c$ (163)	1.59 ± 0.05	0.00 ± 0.05	0.73
CIPS (polar)	428	Cc (9)			1.32
50 $Sb(In)^1$-S	440	$P3$ (143)	1.59 ± 0.04	−0.03 ± 0.00	1.25
50 $Bi(In)^1$-S	440	$P3$ (143)	1.59 ± 0.03	−0.03 ± 0.00	1.50
50 $Sb(P)^A$-S	462	$P1$ (1)	1.64 ± 0.01	0.08 ± 0.13	0.46
50 $As(P)^A$-S	442	$P1$ (1)	1.57 ± 0.02	0.04 ± 0.09	0.99

placement remains high across In-site doping cases, only slightly reduced relative to the undoped structure, confirming that Se lattice adapts dopants without heavily disrupting polar distortion. CIPS shows approximately identical Cu displacements in all In-doped cases, suggesting the stiffer S network constrains both dopant relaxation and Cu off-centering. The largest Δz changes happen in P-site doped structures, mainly with Sb, where both Cu and In displacements increase sharply and stan-

dard deviations widen. This points to greater local asymmetry and lattice strain, especially in low-symmetry (P1) structures. Bi doping in CIPSe leads to more symmetric Cu and In displacements than Sb, likely due to its larger size and stronger coupling with the Se lattice. These patterns highlight (i) CIPSe is structurally more tolerant than CIPS, (ii) Bi dopants induce distortion more coherently than Sb, and (iii) P-site doping perturbs lattice symmetry more than In-site doping.

To see how these displacements change at different cation sites, we take a closer look at the out-of-plane shifts ($\Delta z \pm \sigma$) for Cu, In, P, and dopant atoms in pristine and selected In-site doped structures in Fig. 3. For all structures, Cu shows the largest displacement, supporting its central role in driving ferroelectricity. In CIPSe, Cu Δz stays relatively high after Sb or Bi doping, with only a slight drop from the undoped value, indicating that the softer Se lattice absorbs local strain without strongly affecting Cu off-centering. Cu displacement in CIPS remains nearly constant for In-doped structures, pointing to the rigid S framework resists dopant-induced relaxation. In displacement, however, is more sensitive. Due to stronger local distortion from Bi with larger ionic radii and lone pair activity, In sites in CIPSe shift more with Bi than with Sb. CIPS shows smaller In shifts, reflecting its tighter lattice. The dopants themselves show configuration-dependent behavior. In Sb-doped CIPSe and CIPS, Sb and In displace in opposite directions, creating asymmetry. However, in Bi-doped CIPSe and CIPS, Bi and In shift together, reducing internal strain and maintaining structural coherence. This difference probably arises from the larger ionic radius of Bi^{3+} and its tendency to off-center due to stereochemically active lone pair interactions. These observations highlight how the combined effects of dopant chemistry and lattice stiffness dictate the symmetry and directionality of cation displacements under In-site substitution.

Fig. 4 presents $\Delta z \pm \sigma$ for Cu, In, P, and dopant atoms in pristine and selected P-site doped CIPS and CIPSe structures. Compared to In-site substitution, P-site doping introduces more structural asymmetry, especially in Sb-doped systems. In both lattices, Sb substitution leads to distinct and uneven displacements of nearby cations, with larger Δz values and standard deviations for In and P. These distortions are more noticeable in CIPS, which adopts a low-symmetry P1 structure, while the corresponding Sb-doped CIPSe maintains a higher-symmetry P312 phase. As substitution ends up making the displacements more uniform, particularly in CIPSe, where the softer lattice can better adapt local strain. Cu displacement remains relatively stable for all P-site doped cases, confirming its role as the main contributor to polarization. The data show that P-site substitution interrupts the P–X network more than In-site doping, and the degree of distortion is correlated with both the type of dopant and how rigid the host lattice is.

3.2 Polarization and switching barrier trends

Polarization values (Table 3) calculated from the relaxed structures closely follow the trends observed in Cu displacements. For undoped structures, CIPS has a polarization of 2.8 μC cm^{-2} (close to experimental reports of ~3.5 μC cm^{-2})[35,37,38] and an energy barrier of −0.495 eV between the polar and non-polar states. CIPSe, with its softer lattice, displays a slightly lower polarization (2.42 μC cm^{-2}) and a switching barrier of −0.251 eV. In-site substitutions with Sb and Bi lead to mixed effects. In CIPSe, several doping configurations maintain ferroelectricity, with small but consistent changes in polarization

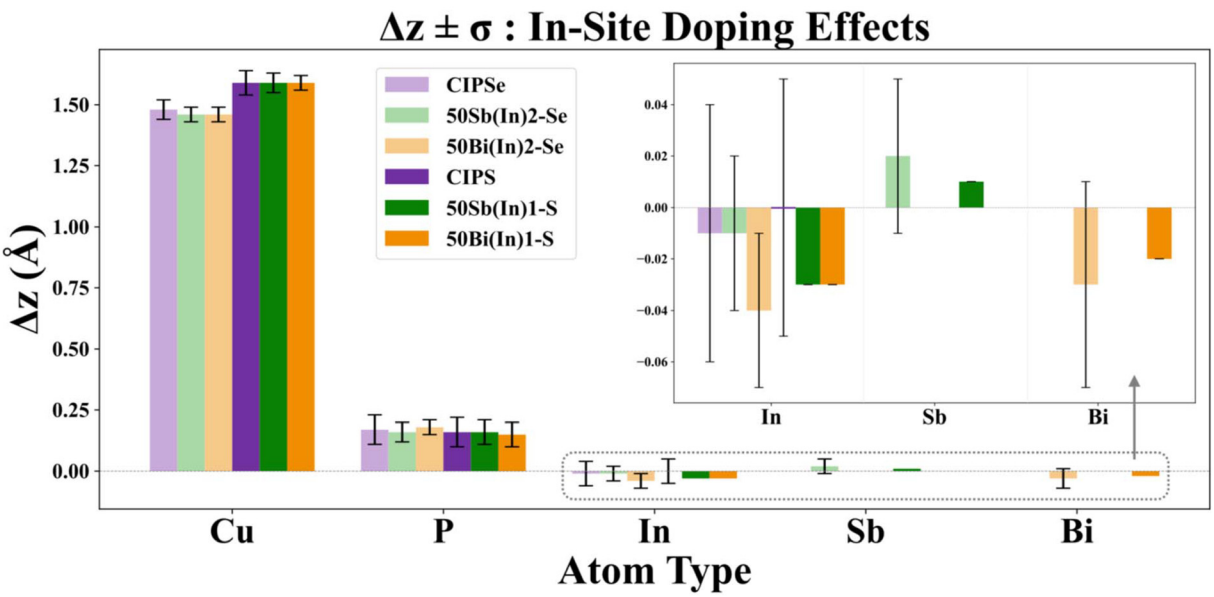

Fig. 3 Out-of-plane atomic displacements ($\Delta z \pm \sigma$) for: Cu, P, In, Sb, and Bi in undoped and selected 50% In-site doped CIPSe and CIPS structures. Top right is an expanded view of the cation displacements, which are two orders of magnitude smaller than the Cu displacements.

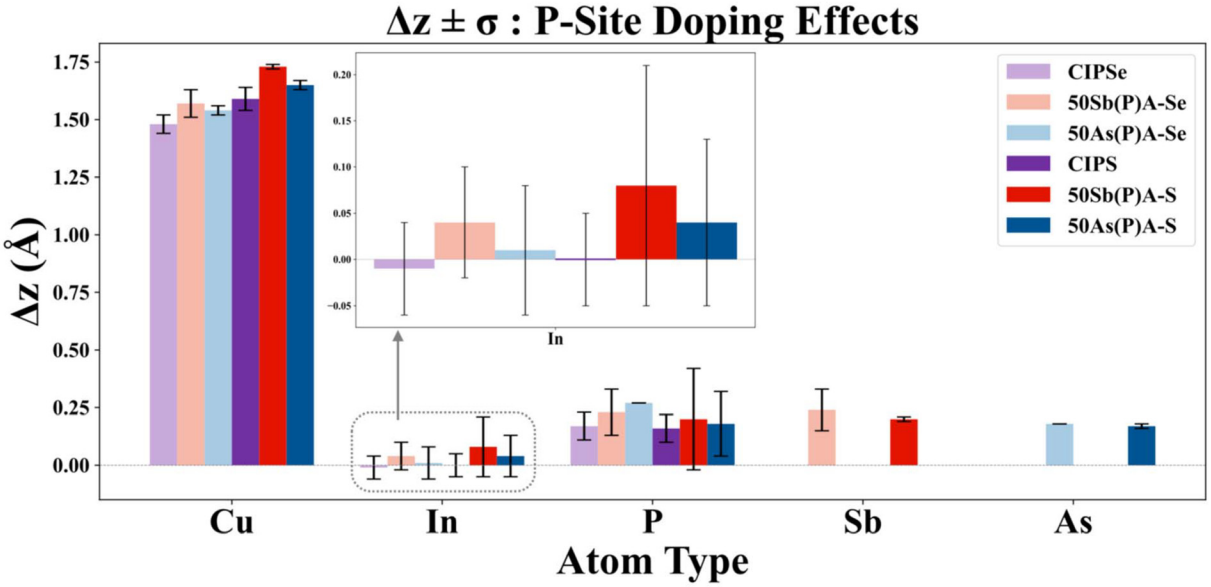

Fig. 4 Out-of-plane atomic displacements ($\Delta z \pm \sigma$) for Cu, In, P, Sb, and As in pristine and selected 50% P-site doped CIPSe and CIPS structures. Top right is an expanded view of the In displacements, which are one or two orders of magnitude smaller than Cu displacements, larger than those in Fig. 3.

Table 3 Polarization (P) and energy barriers ($\Delta E_{f\to p}$) for undoped and doped CIPSe and CIPS under selected In-site and P-site substitutions

CIPSe		P (μC cm^{-2})	$\Delta E_{f\to p}$ (eV)	CIPS		P (μC cm^{-2})	$\Delta E_{f\to p}$ (eV)
Undoped		2.42	−0.251	Undoped		2.80	−0.495
25	Sb(In)–Se	2.40	−0.337	25	Sb(In)–S	2.48	−0.568
50	Sb(In)^{1}–Se	2.48	−0.292	50	Sb(In)^{1}–S	2.33	−0.589
50	Sb(In)^{2}–Se	2.33	−0.278	50	Sb(In)^{2}–S	2.15	−0.390
50	Sb(In)^{3}–Se	2.28	−0.278	50	Sb(In)^{3}–S	2.13	−0.585
75	Sb(In)–Se	2.34	−0.289	75	Sb(In)–S	1.92	−0.367
25	Bi(In)–Se	2.38	−0.279	25	Bi(In)–S	2.51	−0.572
50	Bi(In)^{1}–Se	2.48	−0.322	50	Bi(In)^{1}–S	2.38	−0.592
50	Bi(In)^{2}–Se	2.30	−0.092	50	Bi(In)^{2}–S	2.21	−0.368
50	Bi(In)^{3}–Se	2.25	−0.324	50	Bi(In)^{3}–S	2.21	−0.384
75	Bi(In)–Se	2.33	−0.302	75	Bi(In)–S	2.05	−0.358
50	As(P)^{A}–Se	2.51	−0.282	50	As(P)^{A}–S	2.89	−0.622
50	As(P)^{B}–Se	2.49	−0.330	50	As(P)^{B}–S	2.87	−0.452
100	As(P)–Se	2.66	−0.300	100	As(P)–S	3.08	−0.724
50	Sb(P)^{A}–Se	2.31	−0.251	50	Sb(P)^{A}–S	2.88	−0.575
50	Sb(P)^{B}–Se	2.41	−0.137	50	Sb(P)^{B}–S	2.87	−0.275
100	Sb(P)–Se	2.89	−0.115	100	Sb(P)–S	3.71	−0.388

(±20%) and energy barriers. Results for Bi substitution depends more on how the Bi atoms are arranged. In the 50Bi(In)^{2}-Se configuration, the switching barrier drops to −0.092 eV while polarization remains ~2.30 μC cm^{-2}, indicating that the stereochemical activity of the Bi 6s^{2} lone pair is limited due to a more balanced local environment. This allows orbital decoupling without introducing significant strain. In contrast, other Bi configurations such as 50Bi(In)^{3} show stronger lone pair distortion, leading to deeper energy wells. Sb substitutions, with weaker lone pair effects, tend to preserve more symmetric Cu environments, with polarization and switching barriers close to the undoped case.

In CIPS, for all configurations of Sb/Bi doping at the In-site, the polar structure is preserved, but the polarization decreases more sharply than in the selenide counterpart. This drop, from 2.80 μC cm^{-2} in the pristine structure to a range of 1.92–2.51 μC cm^{-2} in the doped systems, can be attributed to reduced out-of-plane atomic displacements in the stiffer sulfide lattice, which limits structural relaxation around the dopants. The switching barrier lies in the range of −0.590 eV

to −0.350 eV. The Sb and Bi(In)^1–S configurations show the highest barrier (~−0.590 eV), possibly due to their higher trigonal symmetry, which reduces lone pair activity and allows a more coherent off-centering of Cu atoms, consequently stabilizing the polar phase.

For P-site doping, As substitution in CIPS increases polarization from 2.89 μC cm^{-2} at 50As(P)^A–S to 3.08 μC cm^{-2} at 100As(P)–S, which is accompanied by the switching barrier deepening (−0.622 eV to −0.724 eV). This indicates that As maintains the P–S network and enhances the stability of Cu off-centering. By contrast, Sb substitution at the P site also raises polarization substantially, reaching 3.71 μC cm^{-2} at 100% Sb(P)–S, but here the switching barrier decreases (−0.575 eV at 50% → −0.388 eV at 100%), suggesting a flatter double-well and weaker bistability.

In CIPSe, the overall polarizations are lower (~2.3–2.9 μC cm^{-2}) and barriers are markedly smaller (−0.115 to −0.330 eV), when compared to CIPS, showing the softer Se-based lattice. Full Sb substitution produces 2.89 μC cm^{-2} polarization but a very shallow barrier (−0.115 eV), showing that in CIPSe, enhanced polarization often occurs at the expense of bistability. These results support that Cu off-centering remains the primary driver of polarization. However, the effect of substitution depends strongly on lattice rigidity: in CIPS, As at the P-site strengthens both polarization and bistability, while Sb raises polarization but compromises switching stability. In CIPSe, the softer lattice tolerates substitutions more broadly, but shows a tendency to flatten the double-well potential and reduce switching barriers.

3.3 Electronic structure: band structure and PDOS

While ferroelectricity mostly depends on atomic displacements and symmetry breaking, understanding how compositional tuning modifies the band structure and PDOS is essential for enhancing material functionality at the nanoscale. When a material has a very small band gap, free-moving electrons shield the internal electric fields associated with ferroelectricity, causing ferroelectricity to be lost. Conversely, when the band gap is too large, poor carrier mobility can weaken ferroelectric switching.[39,40] This highlights the importance of achieving an optimum balance between structural polarization and electronic band structure to design functional ferroelectric semiconductors for device applications. In this section, we investigate how atomistic substitutions at the In and P sites modify the electronic structure of CIPSe and CIPS, focusing on the influence of dopant chemistry, substitution site selectivity, and lattice flexibility on band edge behavior. Through a comparative analysis of band structures and PDOS, we identify the key factors that control band gap tuning in these layered vdW ferroelectrics.

Experimental optical studies report band gaps of ~2.8 eV for CIPS and ~2.1–2.2 eV for CIPSe.[41] DFT calculations using the PBE functional predict significantly lower values of ~1.0 eV for both materials in their polar phases,[35] reflecting the known band gap underestimation of GGA-based approaches. In our work, we calculate band gaps of 1.32 eV for CIPS and 0.62 eV for CIPSe in their polar undoped structures. Other theoretical studies[35,38] further confirm the semiconducting nature of CIPS and CIPSe, with electronic structures sensitive to lattice flexibility and cation displacements. Our results for CIPSe-based structures show that substituting In sites with Sb or Bi consistently increases the band gap compared to the undoped polar structure, which has an initial value of approximately 0.62 eV. Based on the calculated band structures, this trend is mainly driven by stabilization of the LUMO, with minimal impact on the HOMO. In other words, the LUMO shifts upward significantly, while the HOMO remains largely unchanged, leading to an overall widening of the gap. For Sb substitution, the band gap increases gradually with doping concentration: 25% Sb results in a gap of ~0.74 eV, while 50% Sb yields gaps ranging from ~0.74 eV (50Sb(In)^1–Se) to ~0.92 eV (50Sb(In)^2–Se, the maximum) and ~0.87 eV (50Sb(In)^3–Se). At 75% Sb, the gap remains widened around ~0.87 eV. Bi substitution further enhances the band gap, with values ranging from ~0.90 to ~1.07 eV across 25% to 75% doping levels, again reaching a maximum at 50% doping (50Bi(In)^2–Se). Complete sets of band structures and PDOS plots for all other doped configurations are provided in the SI.

To illustrate these trends, Fig. 5 presents the band structures and PDOS for non-polar, undoped and 50% Bi-doped

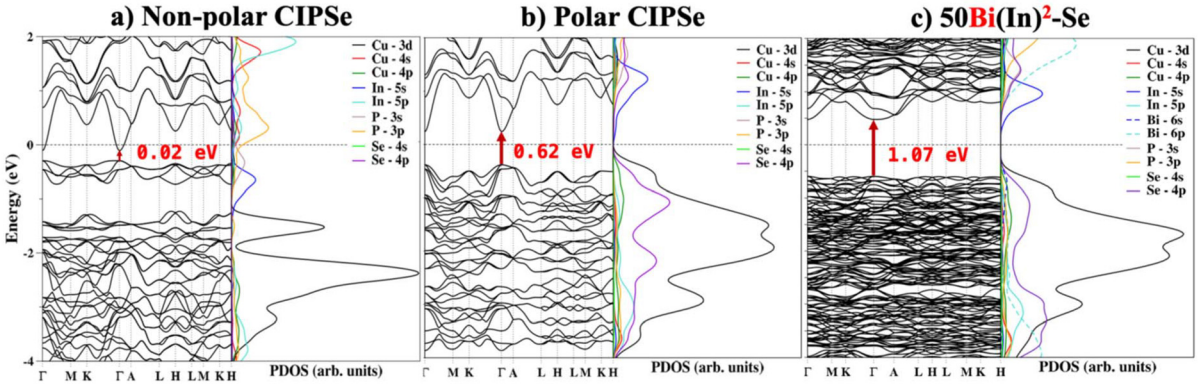

Fig. 5 Band structures and PDOS for CIPSe systems: (a) non-polar undoped, (b) polar undoped, and (c) polar 50Bi(In)^2–Se.

polar CIPSe (50Bi(In)^2–Se). This particular case was chosen because it presents a good balance between widening the band gap and preserving the direct-gap character (Fig. 5c), where the conduction band edge shows increased hybridization between Se 4p and Bi p-states, while In 5s orbitals still contribute significantly. This favorable alignment arises because the p-orbitals of Sb and Bi are energetically close to the Se 4p orbitals, allowing coherent coupling at the LUMO level without disrupting the HOMO. As a result, the LUMO is selectively stabilized, while the HOMO remains largely composed of Cu 3d and Se 4p states. In particular, Bi, with its stereochemically active lone pair, introduces slightly stronger perturbations to the LUMO compared to Sb, justifying the larger band gap expansion observed for Bi doping. Overall, these results demonstrate the intrinsic flexibility of the CIPSe lattice in incorporating dopants without losing semiconducting behavior, highlighting its potential for band gap engineering through controlled compositional tuning.

Substituting P sites in CIPSe with Sb or As leads to an intense reduction in the band gap. For Sb substitution, the gap approaches to near zero for all doping levels, with gaps of only ~0.01–0.02 eV even at 100% substitution. As substitution is less disruptive at 50% doping, where gaps are ~0.32–0.37 eV depending on configuration, but a full 100% As substitution of P results in near-gap closure (~0.004 eV). These trends highlight the critical role of the P–P dimer network in stabilizing the electronic structure in CIPSe. Due to the softer and more polarizable nature of the Se lattice, the P–P bonds act as an essential component supporting the semiconducting state. Partial or complete disruption of this network, especially through Sb or As substitution, destabilizes the system. For compositional design in CIPSe, maintaining the stability of the P–P network is essential to maintain functional electronic properties.

Fig. 6 presents the band structures and PDOS for non-polar, undoped and representative doped polar CIPS systems. These examples highlight the key features discussed, including the effects of doping on band gap behavior and electronic structure. For In-site substitution with Sb/Bi, the valence band edge remains largely composed of Cu 3d and S 3p states, while the conduction band is composed of In 5s and dopant p-states. With increasing Sb or Bi content, a consistent upward shift in the LUMO is observed, and the HOMO remains relatively stable or slightly lowers in energy. This shift leads to a gradual widening of the E_g, from 1.19 eV in 25% Sb to 1.50 eV in 50% Bi cases. These changes are consistent with a reduction in p–d orbital mixing near the Fermi level, caused by the less tightly bound p-orbitals of Sb^{3+} and Bi^{3+} compared to In^{3+}. The wider separation between Cu-derived valence states and Bi/Sb-derived conduction states suggests a more ionic character, effectively stabilizing the insulating state. The increase in band gap is accompanied by a reduction in spontaneous polariz-

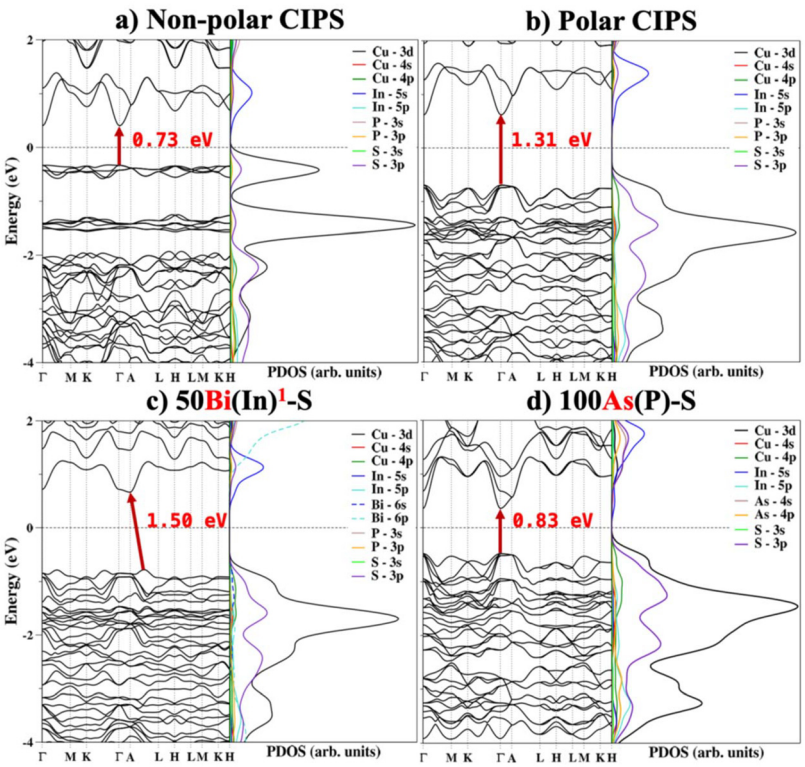

Fig. 6 Calculated band structures and PDOS for CIPS systems: (a) non-polar undoped CIPS, (b) polar undoped CIPS, (c) polar 50% Bi-substituted CIPS at In sites (50Bi(In)^1–S), and (d) polar 100% As-substituted CIPS at P sites. The comparison highlights the effects of In-site and P-site substitution on band gap magnitude, indirect gap formation, and overall electronic structure.

ation (Table 3). The switching barriers remain in a similar range to the undoped case (−0.590 to −0.350 eV), showing that bistability of the polar phase is preserved for all Sb- and Bi-doped configurations. As a result, In-site substitution maintains stable ferroelectric behavior and supports an insulating electronic state.

We note that in some cases (particularly the non-polar phases), the PDOS appears more filled near the gap than the corresponding band dispersions shows. This difference can be referenced to the fact that the band plots reflect eigenvalues along selected k-paths, and the PDOS sums over the entire Brillouin zone using a finite smearing. In cases like non-polar CIPS (Fig. 6a), mid-gap features appear in the PDOS that are used to qualitatively understand the bonding happening close to the Fermi level. These do not result only from numerical broadening. They are also related to actual states at *k*-points not sampled in the band path. In CIPS and CIPSe, Cu-derived states are known to hybridize strongly and are sensitive to site disorder, linking Cu displacements to features in the electronic band structure. Structural studies and prior work have shown that Cu can occupy multiple shallow wells in the lattice,[38] including quasi-octahedral, trigonal, or even interlayer positions leading to intrinsic electronic disorder and the emergence of localized or low-dispersion bands within the gap. We tested multiple smearing levels and fixed occupations for undoped phases. The alignment improved slightly in polar CIPSe with reduced Gaussian smearing (at the cost of enhanced PDOS spectral roughness), but the persistent midgap intensity in non-polar systems is attributed to underbound Cu sites whose coordination is not optimal.

Substitution at the P site leads to a qualitatively different outcome. The introduction of Sb/As interferes with the P–P dimer network, leading to significant changes in the local bonding environment and electronic structure. The HOMO increases significantly, and the LUMO either remains nearly constant or decreases slightly, resulting in a distinct narrowing of the band gap. For the Sb-dopant, it reduces to approximately 0.01 eV for complete P-site substitution, showing significant orbital overlap and a narrow separation between the HOMO and LUMO levels. This is accompanied by an increase in the calculated spontaneous polarization, ∼3.7 μC cm^{-2}. However, this is accompanied by a relatively low switching barrier (∼−0.388 eV), indicating a flattening of the double-well potential. This combination indicates a flattening of the double-well potential and a possible destabilization of long-range ferroelectric order.

Substitution at the P site leads to a qualitatively different outcome. The introduction of Sb or As interferes with the P–P dimer network, inducing significant changes in local bonding and electronic structure. For Sb doping, the HOMO rises considerably, while the LUMO remains nearly constant or slightly lowers, resulting in strong band gap narrowing. In the fully substituted case (100% Sb(P)), the band gap is reduced to ∼0.40 eV, and the calculated spontaneous polarization reaches 3.71 μC cm^{-2}, the highest among all tested structures. However, this is accompanied by a relatively low switching barrier ($\Delta E_f \rightarrow$ p ≈ −0.388 eV), indicating a flattening of the double-well potential and suggesting a potential softening of the ferroelectric phase stability.

In contrast, As dopant (Fig. 6d) offers a more favorable balance. Although it also enhances polarization, reaching up to 3.08 μC cm^{-2}, it prevents full gap closure, maintaining E_g in the range of 0.83–0.99 eV, with a much higher switching barrier ($\Delta E\_f \rightarrow$ p ≈ −0.724 eV), implying a more stable ferroelectric character. As atoms are smaller than Sb and closer in size to P, allowing it to site more smoothly into the P–P bonding network without completely breaking or distorting it. Beyond size, electronegativity compatibility plays an important role in maintaining the electronic symmetry of substituted structures. For example, As (Pauling χ = 2.18) and P (2.19) have nearly identical electronegativity values, supporting similar orbital hybridization and covalent bonding within the P–S framework. This is in contrast to Bi (χ = 2.02) and In (1.78), where the larger electronegativity gap introduces stronger charge redistribution and local symmetry breaking. Such mismatches can enhance lone pair stereoactivity and orbital mixing.

With higher electronegativity, As maintains more covalent bonding with surrounding atoms, better simulating P behavior. Its orbitals also overlap more effectively with P due to their similar sizes, which interacts less aggressively with electronic structure relative to Sb. As a result, As/P CIPS systems keep their structural asymmetry and still support overall electronic stability, showing that ferroelectric switching remains energetically accessible. These features identify As(P) doped CIPS variants as promising systems for further electronic and structural tuning, where partial barrier lowering and controlled band gap reduction can be achieved without loss of switchability or insulating behavior.

A closer look at the band edge positions along the Brillouin zone reveals both CIPS and CIPSe are direct-gap semiconductors at Γ in their pristine and polar forms, but even low levels of In-site doping with Sb or Bi trigger indirect transitions. Structures with 50% Bi doping in CIPSe show a mix of gap characters depending on configuration. In particular, the 50Bi(In)^2–Se (Fig. 5c) regains a direct Γ → Γ gap, and the lowest switching barrier (Table 3). This seems tied to its balanced Bi arrangement in symmetric zig-zag configuration and resulted limited lone pair distortion. Its monoclinic symmetry allows just enough structural adjustment to maintain polarization while shifting the band edges. However, other Bi configurations lead to indirect gaps, highlighting the role of local site asymmetry and dopant placement in determining electronic transition pathways. For example, in 50Bi(In)^3–Se, the lower symmetry allows the Bi 6s^2 lone pair to act more strongly, leading to greater off-centering, a higher switching barrier, and a shift to an indirect band gap. For 50Bi(In)^1–S (Fig. 6c), the tilting of the LUMO at Γ appear because Bi 6p states mix into the conduction band and local lattice distortions from Bi atoms break the symmetry of the electronic potential. Some *k*-directions exhibit stronger Bi 6p–S 3p hybridization, while others retain more In 5s character,

leading to an asymmetric conduction band curvature and shifting the conduction band minimum away from Γ. On the other hand, the downward shift of the HOMO at Γ arises because local lattice distortions from Bi $6s^2$ lone pairs weaken the Cu 3d–S 3p bonding overlap at the zone center. Some *k*-directions maintain stronger Cu 3d–S 3p hybridization, lifting the HOMO energy between A and L and relocating the valence band maximum. In the relatively rigid sulfide lattice of CIPS, these distortions are insufficiently absorbed, leading to enhanced symmetry breaking and further promoting indirect gap formation. In contrast, the softer and more polarizable CIPSe lattice can more readily adjust to similar Bi or Sb substitutions, allowing CIPSe to maintain a direct band gap character while still achieving band gap widening through controlled compositional tuning. P-site substituted structures, consistently maintain direct transitions, highlighting the role of the P–P dimer in electronic symmetry.

Comparing PDOS and band structure results for sulfide and selenide-based structures shows that Bi doping leads to a larger band gap than Sb in both systems. This comes from the larger radius of Bi and its active $6s^2$ lone pair, which pushes up the conduction band and widens the gap. In contrast, Sb^{3+}, with a radius close to In^{3+}, causes less lattice distortion but allows stronger hybridization with nearby Cu and P/S/Se states. This hybridization near the valence band edge narrows the gap in Sb-doped structures. These trends show that both ionic size and orbital chemistry control how the band gap evolves, offering ways to tune electronic properties while keeping ferroelectricity preserved. Also, P-site substitution is not a good strategy for softer lattices like CIPSe, where the structure cannot effectively control dopant displacement (Fig. 4) or bonding asymmetry. Conversely, in more rigid systems like CIPS, choosing a dopant with similar electronegativity and atomic size to the host atom provides a useful design rule for tuning band gap and polarization without losing functional stability.

4. Conclusions

In this work, we investigated how compositional tuning modifies the structure, polarization, and electronic properties of $CuInP_2X_6$ (X = Se, S) layered ferroelectrics using DFT-based substitution of In → Sb/Bi and P → As/Sb. Applying the same substitutions for both chalcogen systems, we identified how lattice softness, dopant chemistry, and cation placement govern the balance between structural stability, switchability, and semiconducting behavior. CIPSe, with its softer and more polarizable Se lattice, consistently shows more tolerance to chemical substitution. In-site doping with Bi or Sb maintains Cu off-centering and allows systematic band gap increases (up to ~1.07 eV), particularly when Bi is arranged in a zigzag pattern that distributes strain evenly in the lattice, creating a form of balance within distortion.

For CIPS, although some dopant configurations reduce polarization, others, particularly at the P site, support or even enhance it. Band gap tunability in CIPS is also more extensive than in CIPSe, with both widening (Bi/In substitutions) and narrowing (P-site dopants) possible depending on dopant type and arrangement. P-site substitution tends to introduce stronger structural and electronic distortions than In substitutions. In CIPSe, the weaker P–P dimer network is destabilized by larger dopants like Sb.

The trends can be summarized in using our calculated structure–property relationships. In-site Bi substitution increases E_g and maintains ferroelectricity, but P-site Sb collapses E_g by disrupting structural symmetry. As is found to be a more balanced dopant that maintains both polarization and semiconducting character in CIPS, though not in CIPSe. These comparisons highlight that successful band gap tuning is both site-specific and configuration-sensitive, driven by local geometry, bonding compatibility, and the ability of host lattice to adjust strain and maintain symmetry.

In both systems, three chemical design factors stand out as key determinants of structure–property relationships: ionic radius mismatch, electronegativity compatibility, and stereochemical lone pair activity. Larger, stereoactive cations (like Bi^{3+}) can widen the gap and shift electronic symmetry, but only when lattice strain is minimized through symmetric placement. Substitutions closer in size and electronegativity to the host atom, such as As for P (χ = 2.18 *vs.* 2.19), tend to maintain structural order and bonding coherence more effectively. These insights suggest that future design of 2D vdW ferroelectrics should not only consider dopant charge and concentration, but also match with the host atom in valence configuration, local bonding environment, and lattice symmetry constraints. Incorporating d-block or f-block elements with active orbitals or spin states could offer new pathways for coupling ferroic and electronic order. Moreover, understanding how lone pair activity interacts with lattice rigidity can inform how we approach designing soft ferroelectric semiconductors that combine tunable band gaps with low switching barriers.

Author contributions

ML: conceptualization, investigation, methodology, data curation, formal analysis, writing – original draft, writing – review & editing, visualization. JWB: conceptualization, methodology, writing – review and editing, supervision, project administration, funding acquisition.

Conflicts of interest

The authors declare no competing financial interest.

Data availability

Example input and output files to support the findings of this study are openly available at: **https://github.com/bennettlabs-UMBC/2D-vdW-Comp-Tuning**. All calculations employed the

open source plane wave package Quantum Espresso, available at: **https://www.quantum-espresso.org/**. All open source pseudopotentials used in this study were the GBRV high-throughput set, available at: **https://www.physics.Rutgers.edu/gbrv/**.

Supplementary information: DFT structural relaxations and electronic band structure results. See DOI: **https://doi.org/10.1039/d5dt01674f**.

Acknowledgements

The authors wish to acknowledge DTRA through grant number HDTRA12410015. Calculations were performed, in part, using the UMBC High Performance Computing Facility (HPCF), supported by the National Science Foundation under the MRI grants CNS-0821258, CNS-1228778, and OAC-1726023 and the SCREMS grant DMS-0821311. This research used the Theory and Computation facility of the Center for Functional Nanomaterials (CFN), which is a U.S. Department of Energy Office of Science User Facility, at Brookhaven National Laboratory under Contract No. DE-SC0012704.

References

1 X. Wang, Y. Sun and K. Liu, *2D Mater.*, 2019, **6**, 042001.
2 V. Yu. Verchenko, A. V. Kanibolotskiy, A. V. Bogach, K. O. Znamenkov and A. V. Shevelkov, *Dalton Trans.*, 2022, **51**, 8454–8460.
3 V. Yu. Verchenko, A. V. Stepanova, A. V. Bogach, M. A. Kirsanova and A. V. Shevelkov, *Dalton Trans.*, 2023, **52**, 5534–5544.
4 A. Simon, J. Ravez, V. Maisonneuve, C. Payen and V. B. Cajipe, *Chem. Mater.*, 1994, **6**, 1575–1580.
5 F. Liu, L. You, K. L. Seyler, X. Li, P. Yu, J. Lin, X. Wang, J. Zhou, H. Wang and H. He, *Nat. Commun.*, 2016, **7**, 1–6.
6 V. Maisonneuve, V. Cajipe, A. Simon, R. Von Der Muhll and J. Ravez, *Phys. Rev. B:Condens. Matter Mater. Phys.*, 1997, **56**, 10860.
7 V. Liubachko, V. Shvalya, A. Oleaga, A. Salazar, A. Kohutych, A. Pogodin and Yu. M. Vysochanskii, *J. Phys. Chem. Solids*, 2017, **111**, 324–327.
8 C.-H. Chiang, C.-C. Lin, Y.-C. Lin, C.-Y. Huang, C.-H. Lin, Y.-J. Chen, T.-R. Ko, H.-L. Wu, W.-Y. Tzeng, S.-Z. Ho, Y.-C. Chen, C.-H. Ho, C.-J. Yang, Z.-W. Cyue, C.-L. Dong, C.-W. Luo, C.-C. Chen and C.-W. Chen, *J. Am. Chem. Soc.*, 2024, **146**, 23278–23288.
9 X. Bourdon, V. Maisonneuve, V. B. Cajipe, C. Payen and J. E. Fischer, *J. Alloys Compd.*, 1999, **283**, 122–127.
10 A. Dziaugys, K. Kelley, J. A. Brehm, L. Tao, A. Puretzky, T. Feng, A. O'Hara, S. Neumayer, M. Chyasnavichyus, E. A. Eliseev, J. Banys, Y. Vysochanskii, F. Ye, B. C. Chakoumakos, M. A. Susner, M. A. McGuire, S. V. Kalinin, P. Ganesh, N. Balke, S. T. Pantelides, A. N. Morozovska and P. Maksymovych, *Nat. Commun.*, 2020, **11**, 3623.
11 F. Sun, H. Xu, W. Hong, Z. Sun and W. Liu, *Adv. Funct. Mater.*, 2024, **34**, 2313776.
12 C. Guo, J. Zhu, X. Liang, C. Wen, J. Xie, C. Gu and W. Hu, *Nat. Commun.*, 2024, **15**, 10152.
13 D. Wijethunge, C. Tang, C. Zhang, L. Zhang, X. Mao and A. Du, *Appl. Surf. Sci.*, 2020, **513**, 145817.
14 P. D. Taylor, S. A. Tawfik and M. J. S. Spencer, *Nanotechnology*, 2023, **34**, 065701.
15 F. Kong, L. Zhang, T. Cong, Z. Wu, K. Liu, C. Sun, L. Pan and D. Li, *J. Appl. Phys.*, 2022, **132**, 044103.
16 K. Cho, S. Lee, R. Kalaivanan, R. Sankar, K. Choi and S. Park, *Adv Funct. Mater.*, 2022, **32**, 2204214.
17 C. B. Park, A. Shahee, K. Kim, D. R. Patil, S. A. Guda, N. Ter-Oganessian and K. H. Kim, *Adv. Electron. Mater.*, 2022, **8**, 2101072.
18 X. Wang, Z. Shang, C. Zhang, J. Kang, T. Liu, X. Wang, S. Chen, H. Liu, W. Tang, Y.-J. Zeng, J. Guo, Z. Cheng, L. Liu, D. Pan, S. Tong, B. Wu, Y. Xie, G. Wang, J. Deng, T. Zhai, H.-X. Deng, J. Hong and J. Zhao, *Nat. Commun.*, 2023, **14**, 840.
19 A. Galdámez, V. Manríquez, J. Kasaneva and R. E. Avila, *Mater. Res. Bull.*, 2003, **38**, 1063–1072.
20 P. Yan, M. Layegh, R. Stadel, J. Birenzvige, P. Y. Zavalij, E. E. Rodriguez and J. W. Bennett, *Chem. Mater.*, 2025, **37**, 5086–5098.
21 Y. Ma, Y. Yan, L. Luo, S. Pazos, C. Zhang, X. Lv, M. Chen, C. Liu, Y. Wang, A. Chen, Y. Li, D. Zheng, R. Lin, H. Algaidi, M. Sun, J. Z. Liu, S. Tu, H. N. Alshareef, C. Gong, M. Lanza, F. Xue and X. Zhang, *Nat. Commun.*, 2023, **14**, 7891.
22 M. A. Gave, D. Bilc, S. D. Mahanti, J. D. Breshears and M. G. Kanatzidis, *Inorg. Chem.*, 2005, **44**, 5293–5303.
23 G. Kliche, *Z. Naturforsch., A:Phys. Sci.*, 1983, **38**, 1133–1137.
24 R. D. Shannon and C. T. Prewitt, *Acta Crystallogr., Sect. B*, 1969, **25**, 925–946.
25 R. D. Shannon and C. T. Prewitt, *Acta Crystallogr., Sect. B*, 1970, **26**, 1046–1048.
26 P. Giannozzi, S. Baroni, N. Bonini, M. Calandra, R. Car, C. Cavazzoni, D. Ceresoli, G. L. Chiarotti, M. Cococcioni and I. Dabo, *J. Phys.: Condens. Matter*, 2009, **21**, 395502.
27 P. Giannozzi, O. Andreussi, T. Brumme, O. Bunau, M. B. Nardelli, M. Calandra, R. Car, C. Cavazzoni, D. Ceresoli and M. Cococcioni, *J. Phys.: Condens. Matter*, 2017, **29**, 465901.
28 K. F. Garrity, J. W. Bennett, K. M. Rabe and D. Vanderbilt, *Comput. Mater. Sci.*, 2014, **81**, 446–452.
29 D. Vanderbilt, *Phys. Rev. B:Condens. Matter Mater. Phys.*, 1990, **41**, 7892–7895.
30 J. P. Perdew, K. Burke and M. Ernzerhof, *Phys. Rev. Lett.*, 1996, **77**, 3865–3868.
31 S. Grimme, *J. Comput. Chem.*, 2006, **27**, 1787–1799.
32 R. Resta, *Rev. Mod. Phys.*, 1994, **66**, 899–915.
33 R. Resta and D. Vanderbilt, in *Physics of Ferroelectrics: A Modern Perspective*, Springer Berlin Heidelberg, Berlin, Heidelberg, 2007, pp. 31–68.

34 M. Layegh and J. W. Bennett, *J. Chem. Educ.*, 2025, **102**(5), 1803–1813.
35 S. A. Tawfik, J. R. Reimers, C. Stampfl and M. J. Ford, *J. Phys. Chem. C*, 2018, **122**, 22675–22687.
36 T. Babuka, K. Glukhov, Yu. Vysochanskii and M. Makowska-Janusik, *Phase Transitions*, 2019, **92**, 440–450.
37 L. You, Y. Zhang, S. Zhou, A. Chaturvedi, S. A. Morris, F. Liu, L. Chang, D. Ichinose, H. Funakubo, W. Hu, T. Wu, Z. Liu, S. Dong and J. Wang, *Sci. Adv.*, 2019, **5**, eaav3780.
38 J. A. Brehm, S. M. Neumayer, L. Tao, A. O'Hara, M. Chyasnavichus, M. A. Susner, M. A. McGuire, S. V. Kalinin, S. Jesse, P. Ganesh, S. T. Pantelides, P. Maksymovych and N. Balke, *Nat. Mater.*, 2020, **19**, 43–48.
39 A. M. Kolpak, I. Grinberg and A. M. Rappe, *Phys. Rev. Lett.*, 2007, **98**, 166101.
40 M. Dawber, K. M. Rabe and J. F. Scott, *Rev. Mod. Phys.*, 2005, **77**, 1083–1130.
41 I. P. Studenyak, O. A. Mykajlo, V. O. Stephanovich, M. I. Gurzan, Yu. M. Vysochanskii and V. B. Cajipe, *Phys. Status Solidi A*, 2003, **198**, 487–494.